

The mystery of evaporative fluxes surpassing the kinetic limit is revealed: The adsorbed layer evaporates

Yigit Akkus^{1,2}, Anil Koklu¹, Ali Beskok^{1,*}

¹Lyle School of Engineering, Southern Methodist University, Dallas, Texas 75205, USA

²ASELSAN Inc., 06172 Yenimahalle, Ankara, Turkey

Capillary evaporation and the associated passive liquid flow are vital for numerous natural and artificial processes such as transpiration of water in plants¹, solar steam generation²⁻³, water desalination⁴, microfluidic pumping⁵ and cooling of electronic and photonic devices⁶. Recent experiments conducted in nano- and angstrom-scale conduits have shown evaporation rates corresponding to heat fluxes that are one to two orders of magnitude larger than the kinetic theory limit^{7,8}. The physical mechanism elucidating these enormous evaporation rates remains vague. Here we report the discovery of lateral momentum transport within and associated net evaporation from adsorbed liquid layers, which are long believed to be at the equilibrium established between equal rates of evaporation and condensation⁹. Contribution of evaporation from the adsorbed layer increases the effective evaporation area, rendering the excessively estimated evaporative heat flux values below the kinetic theory limit. This work takes the first step towards a comprehensive understanding of atomic/molecular scale interfacial transport at extended evaporating menisci. The modeling strategy used in this study opens an opportunity for computational experimentation of steady-state evaporation and condensation at liquid/vapor interfaces located in capillary nano-conduits.

As the juncture of three phases of matter, contact line has been the subject of countless studies in various disciplines of science. Regardless of the process or the geometrical configuration, studies on evaporation focus on identification and characterization of heat transfer and flow dynamics at the vicinity of the contact line. Fig. 1a-c and Fig. 1d-f show different evaporation processes *in situ* and schematically, respectively. Green dashed rectangles on Fig. 1d-f point out the liquid film distribution around the contact line, which is broadly composed of three multiscale regions as shown in Fig. 1g. Evaporation rate intensifies in evaporating thin film region due to the micro-scale liquid film thickness. The adsorbed nano-scale layer extending further is assumed to be non-evaporating due to the suppression of evaporation by strong long-range intermolecular forces⁹.

While the kinetic theory of gases is widely used to predict the theoretical maximum rate of evaporation, experiments have always calculated smaller heat fluxes than the kinetic limit¹⁰. However, two recent experimental studies have attracted the attention of scientific community by reporting evaporation fluxes one to two orders of magnitude higher than the prediction of kinetic theory^{7,8}. These unexpectedly high flux values were attributed to the possible underestimation of evaporation area in the first study⁷, where the stretching of water meniscus over the flat surface adjacent to the channel mouth was speculated. On the other hand, the second study⁸, reported evaporation rates from a water meniscus located at a channel entrance defined by four sharp edges, which eliminates the possibility of outstretching of the meniscus. Moreover, extension of meniscus

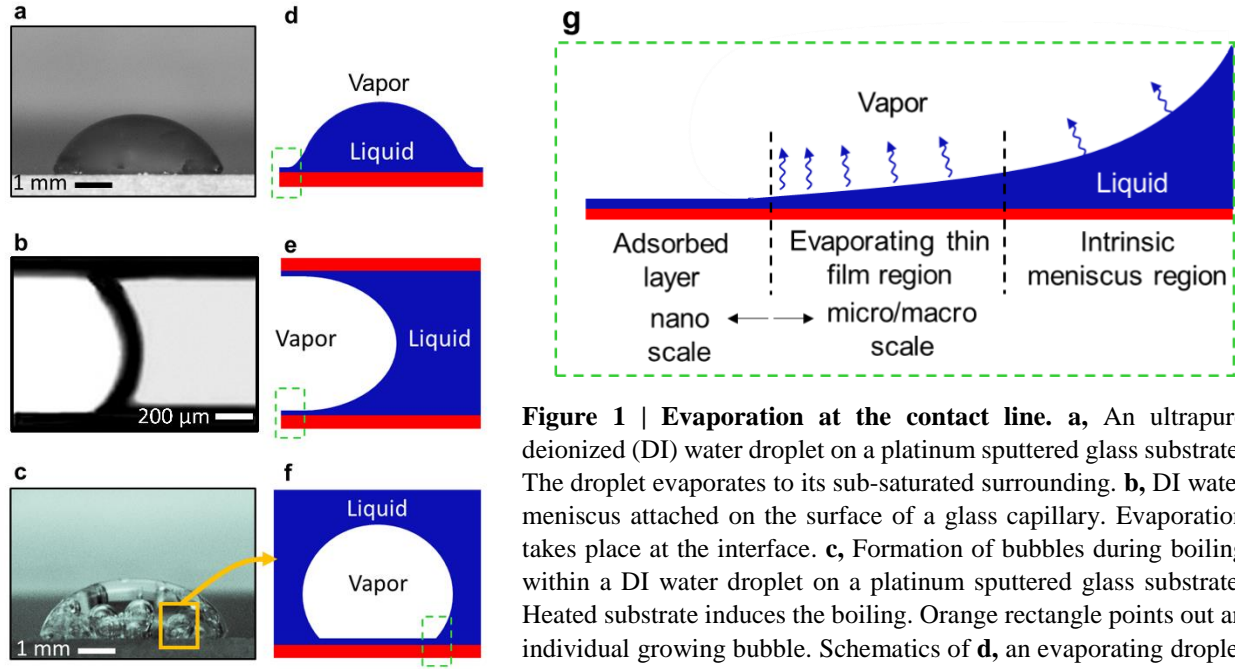


Figure 1 | Evaporation at the contact line. **a**, An ultrapure deionized (DI) water droplet on a platinum sputtered glass substrate. The droplet evaporates to its sub-saturated surrounding. **b**, DI water meniscus attached on the surface of a glass capillary. Evaporation takes place at the interface. **c**, Formation of bubbles during boiling within a DI water droplet on a platinum sputtered glass substrate. Heated substrate induces the boiling. Orange rectangle points out an individual growing bubble. Schematics of **d**, an evaporating droplet **e**, evaporation from a capillary and **f**, bubble growth. Green dashed

rectangles point out the region near contact line, where evaporation rate intensifies due to the decreased liquid film thickness. **g**, Liquid film distribution near the contact line. Liquid forms three multiscale regions around the contact line. Film thickness is at the macro-scale within intrinsic meniscus region. Capillary pressure gradient, arising from the curvature changes, drive the flow in this bulk region. Film thickness is at the micro-scale within evaporating thin film region, where evaporation rate intensifies due to the reduced film resistance. Changes in capillary and disjoining pressures govern the liquid flow in this region. Film thickness is at the nano-scale within adsorbed layer, which is assumed to be non-evaporating due to the suppression of evaporation by strong long-range intermolecular forces.

within the channel was also estimated using a model in the literature⁹, and the evaporation area was modified accordingly. Regardless of the increased evaporation area, estimated heat fluxes still exceeded the kinetic theory limit, indicating the need for fully understanding the characteristics of an evaporating contact line. Undoubtedly, an accurate calculation of the evaporation flux depends on the precise estimation of effective surface area of evaporation, which is extremely challenging to quantify due to lack of information about the molecular/atomic nature of evaporating contact line¹¹. Thermal scientists have long believed that adsorbed tail of the evaporating contact line does not possess a net evaporation rate. While theoretical studies assumed a balance between evaporation and condensation rates and calculated the equilibrium adsorbed film thickness based on the minimum free energy principle⁹, a considerable amount of experimental effort has been devoted to observe the vicinity of contact line¹²⁻¹³. Most recently, Mehrizi and Wang detected extremely stretched nano-films of thickness 2-6 nm attached to a water droplet evaporating to its vapor, and 0-10 nm film attached to a formamide droplet evaporating in air¹⁴. Morphological distinction between intrinsic meniscus and nano-films was apparent in their all experiments. Therefore, they defined the contact line as the intersection of intrinsic meniscus and the nano-film¹⁴. Within the water nano-film, they detected a thinning transition film close to the contact line and a near constant thickness adsorbed film attached to the end of transition film. They characterized the transition film as evaporating due to its thickness variation and adsorbed region

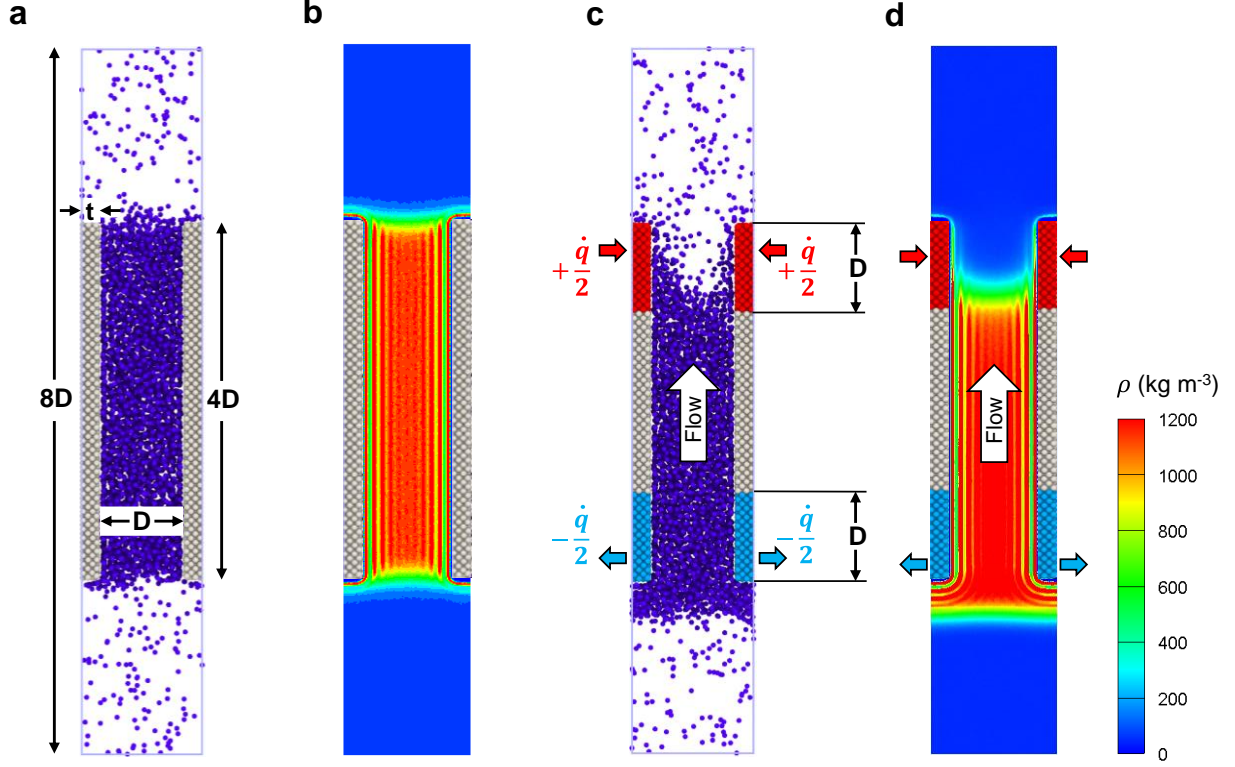


Figure 2 | Computational setup. A snapshot of the isothermal configuration (a). Liquid phase of the saturated Argon mixture (blue spheres) confined between solid Platinum walls (gray spheres). Distance between the channel walls, D , is 3.92 nm and the length of the channel wall and simulation domain is proportional as shown in the figure. Depth of the simulation domain is 3.72 nm. The walls consist of 4 atom layers and has a thickness of $t=0.59$ nm. See Methods section ‘Molecular dynamics simulations’ for further details about the computational setup and simulation procedure. **b**, Density distribution of the isothermal configuration. Two symmetric and statistically stable liquid/vapor interfaces form at the channel inlets. Density layering is prominent near the walls due to the wall force field effect. **c**, A snapshot during the equal energy injection/extraction process. Red and blue parts of the wall show the heating and cooling zones, respectively. The length of these parts is equal to the channel height. The interface at the heating zone is carved due to the evaporative mass loss, while the interface at the cooling zone is expanded due to the condensing fluid atoms. A passive steady liquid flow from the condensing to evaporating interface is initiated due to capillary pumping and molecular diffusion processes¹⁶. **d**, Density distribution during the equal energy injection/extraction. Both interfaces are statistically stable. The evaporating interface is detached from the channel inlet and receded into the channel. The condensing interface is pushed away from the channel inlet and is nearly flat. Density profiles in **b** and **d** were obtained after time averaging of MD results.

as non-evaporating due to its near flat profile. Due to the observation of long nano-films beyond the contact line, we consider this experimental work¹⁴ as a clue to reveal recently reported unexplained evaporation rates^{7,8}. However, identification of effective evaporation area, especially in a few nanometers or sub-nanometer interfaces, where adsorbed film, transition film and intrinsic region are intertwined, is impractical for optical and electron microscopy, because of their nano-scale resolution and operating conditions. Therefore, a comprehensive description of evaporation mechanism at this scale is missing.

To grasp the physical mechanism of evaporation in capillary nano-conduits, we used molecular dynamics (MD), which is a common tool to study the physical movement of atoms and molecules. Although MD simulations are suitable for nano-scale physical and temporal dimensions, MD

results can be successfully used to predict experimentally determined macro-scale system properties¹⁵. Evaporation from an interface can be triggered by two basic approaches. First is to make the system sub-saturated by removing vapor as performed by the experiments^{7,8}. Second is to inject energy to the interface molecules by external heating to increase the interface pressure. Modeling of the first mechanism is not practical for an MD simulation (Methods section ‘Molecular dynamics simulations’). The second mechanism, on the other hand, is realizable as long as the thermodynamic equilibrium of entire system is maintained. To sustain a stable evaporating interface with associated steady-state passive liquid flow, we follow the phase-change driven pumping methodology developed recently¹⁶. First, two symmetric isothermal meniscus structures are created within two parallel Platinum walls by condensation of saturated Argon mixture to the liquid phase due to the interaction between fluid and solid wall atoms, whereas vapor phase of Argon occupies rest of the simulation domain (Fig. 2a-b). Then, equal energy injection/extraction process is applied to solid atoms in the heating/cooling zones located at the opposite ends of the nanochannel (Fig. 2c-d). This approach preserves the thermodynamic state of the mixture by ensuring zero net heat transfer to the system. At the end of 40 ns simultaneous heating/cooling, an extended meniscus and a flat liquid film (both statistically stationary) evolve at the heated and cooled zones of nanochannel, respectively (Fig. 2d). The passive liquid flow through channel is also steady (Methods section ‘Molecular dynamics simulations’). The methodology and the effect of cutoff density for the interface detection are described in ‘Interface detection’ in the Methods section.

Location and morphology of the evaporating meniscus are functions of the heating rate. While a slight heating yields a negligible meniscus deformation, excessive heating results in burnout of the heated wall. During simulations, we applied different heating rates to observe the response of evaporating meniscus. Location and profile of evaporating meniscus corresponding to different heating loads are determined and qualitatively compared with the results of a recent modeling study¹⁷ (Extended Data Fig. 1). The profile shown in Fig. 3a evolves under the highest heating rate just before the burnout of wall. At this heating rate, liquid meniscus is detached from the channel tips and receded into channel. However, a thin monolayer still covers the surface of the channel at both inside and side walls. We consider this monolayer as the adsorbed layer due to its near flat thickness along the inner wall (4.116 ± 0.392 Å) and side wall (2.744 ± 0.196 Å) surfaces. Close-up view of adsorbed layer is shown in Fig. 3b. To investigate the possible momentum transport within the adsorbed layer, mass flow is calculated along the surface coordinate, ‘s’ (see Methods section ‘Mass flow through adsorbed region’). Strikingly, an atomic level mass flow is apparent within the adsorbed layer as shown in Fig. 3c. The mass flow decreases continuously along the layer, which proves evaporation from the adsorbed layers, and vanishes at the end of the side wall, where actually two opposite molecular streams merge due to the periodic boundary condition (Extended Data Fig. 2).

In our computational experiments, we used Argon as the fluid, due to its suitability to be modelled by Lennard-Jones potential with well-defined atomic interactions¹⁸ and its high volatility, which enables statistical averaging for vapor pressure in contrast to water (see Methods section ‘Modeling strategy’). As solid substrate material, we used Platinum due to its empirically defined interaction parameters¹⁹ (see Methods section ‘Molecular dynamics simulations’) and its argon-

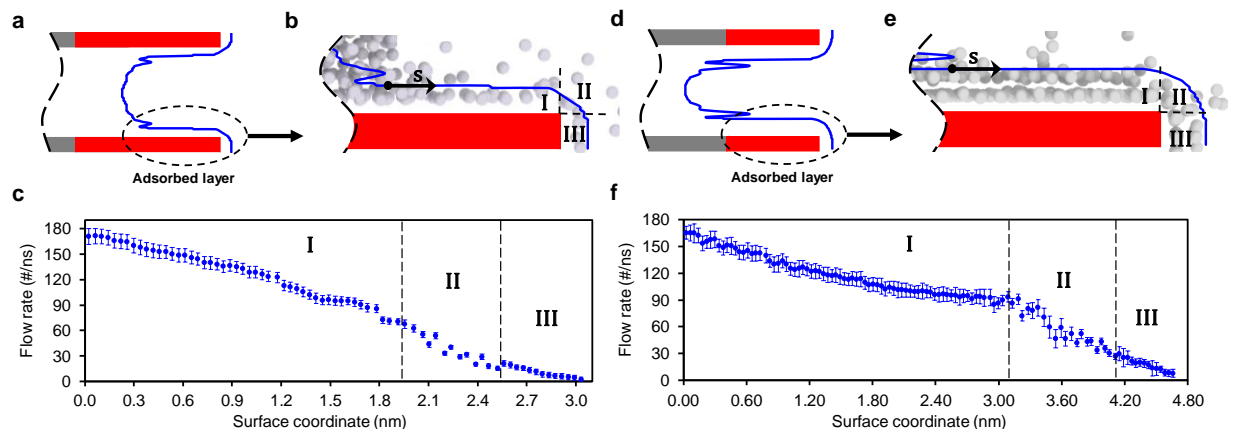


Figure 3 | Evaporating meniscus profiles and mass flow through adsorbed layers. Liquid/vapor interface profile for the first simulation (a). Constant energy is being injected in the red colored walls. Blue line shows the interface. Meniscus is receded into the channel and located within the heating zone. Symmetric adsorbed layers are attached to the meniscus at the channel walls. b, Close-up view of adsorbed layer. An instant capture of atoms is superpositioned on the time-averaged profile of adsorbed layer, which consists of monolayer of fluid atoms. Surface coordinate, ‘s’, follows the interface of adsorbed layer. Regions I, II and III show the adsorbed layer segments located on the inner channel wall, corner and side wall, respectively. c, Mass flow rate along the adsorbed layer. Mass flow rate steadily decreases along the adsorbed layer and vanishes at the stagnation plane located at the end of region III (see Extended Data Fig. 2). The rate of mass loss is equal to the evaporation rate from the adsorbed layer. d, Liquid/vapor interface profile for the second simulation. Meniscus is receded further into channel and located beyond the heating zone. Symmetric adsorbed layers are attached to the meniscus at the channel walls. e, Close-up view of adsorbed layer. Adsorbed layer consists of bilayer of fluid atoms due to increased fluid-wall binding energy. f, Mass flow rate along the adsorbed layer. Mass flow rate decreases along the adsorbed layer. The rate of mass loss (i.e. evaporation rate) is higher at the corner (region II).

philic characteristics. It should be noted that the pumping mechanism used in the simulations requires proper wetting of the wall to keep the liquid phase within channel, otherwise condensed liquid slides over walls and leaves the channel, which prevents the investigation of argon-phobic systems. However, the effect of elevated argon-philicity can be easily examined by increasing the interaction strength between fluid and solid atoms. Fig. 3d shows the profile of evaporating meniscus in the second simulation, where fluid-wall binding energy is 10 times increased. Due to the increased interaction, thickness of adsorbed layer is almost doubled (inner wall: 7.840 ± 0.392 Å, side wall: 6.272 ± 0.196 Å) enabling the formation of a second atomic layer on the first one (Fig. 3e). Surprisingly, the highest attainable heating rate before burnout is nearly doubled and the amount of evaporation from the adsorbed layer remains almost constant at approximately 170 molecules per second (Fig. 3f), despite of the increased attraction between fluid and wall atoms, which is supposed to prevent evaporation. This interesting observation, indeed, is related to the mobility of adsorbed layer even at the elevated attractive forces. Although the first atomic layer (closest to the wall) has low mobility under the effect of wall force field, the second layer is subjected to lesser attraction of solid atoms due to increased distance from the wall, and has high mobility similar to the monolayer formed on the wall in previous simulation.

Our simulations have demonstrated that effective evaporation area can be much larger than the liquid meniscus area due to the evaporation from adsorbed layers. To quantify the effect of evaporation area selection on the heat flux estimations, we calculate the evaporative heat flux for

the first simulation using three different evaporation areas (Extended Data Fig. 3), which yield: (a) $3311 \text{ kg s}^{-1} \text{ m}^{-2}$ for the cross sectional area the between channel walls; (b) $3792 \text{ kg s}^{-1} \text{ m}^{-2}$ for the liquid meniscus area based on a curve fit to liquid/vapor interface; (c) $1386 \text{ kg s}^{-1} \text{ m}^{-2}$ for the total liquid/vapor interfacial area including the adsorbed layer interface. Moreover, an upper bound for the evaporation is estimated based on the kinetic theory (see Methods section ‘Kinetic limit of evaporation’). While the first two area selections result in higher flux values, inclusion of adsorbed layer render the heat flux to a smaller value than the estimated upper bound ($3235 \text{ kg s}^{-1} \text{ m}^{-2}$). Considering the direct observation of extremely stretched nano-films attached to the contact line of evaporating water droplets¹⁴ together with our simulations, the excessive heat fluxes reported in recent experiments^{7,8} can be illuminated. In the first study⁷, a long evaporating adsorbed layer should form on the flat surface adjacent to channel mouth. Therefore, the effective evaporation area should be scaled considering the adsorbed layer length outside the capillary mouth, which would make the evaporative flux smaller than kinetic limit. In the second study⁸, outstretching of meniscus was not expected due to sharp edges at the channel entrance. However, our simulations revealed that evaporating adsorbed layers are able to turn sharp corners and spread over the side walls. Therefore, effective evaporation area should be larger than the cross sectional area of their channels, which can drop the reported heat flux below the kinetic limit.

Discovery of lateral molecular transport within adsorbed layers requires the questioning of previous modeling attempts. In fact, to date, we are unaware of any studies which can construct a molecular model for steady-state evaporating meniscus except two studies^{20,21}. While the latter study was not aiming to construct an adsorbed layer, the former one speculated on the existence of a quasi-crystalline region at the end of the evaporating meniscus due to the vanishing liquid flow. However, extinction of liquid flow does not necessarily imply a quasi-crystalline region, since an opposing cross flow (from the image of simulation domain) merge at the side boundary due to the application of periodic boundary condition, which, in fact, renders the side boundary to a stagnation plane.

Our computational experiments demonstrated that adsorbed liquid films attached to liquid/vapor interfaces are able to spread over long distances, transport momentum and evaporate. Although the amount of liquid evaporating from adsorbed layers is negligible for macroscopic systems, this amount is comparable to the total evaporation for systems having a few nanometers or sub-nanometer interfaces. Therefore, precise calculation of evaporation rates in these scales requires atomic modeling of liquid/vapor interfaces. Our computational setup allows steady-state evaporating and condensing liquid/vapor interfaces located in capillary nano-conduits, making it a useful tool for investigating phase change processes at the nano-scale.

Acknowledgements: Y.A. acknowledges the financial support of ASELSAN Inc. under scholarship program for postgraduate studies. Computations were carried out using high performance computing facilities of Center for Scientific Computation at Southern Methodist University.

* Author to whom correspondence should be addressed. Electronic mail: abeskok@smu.edu

References:

1. Wheeler, T. D. & Stroock, A. D. The transpiration of water at negative pressures in a synthetic tree. *Nature* **455**, 208-212 (2008).
2. Ghasemi, H. *et al.* Solar steam generation by heat localization. *Nat. Commun.* **5**, 4449 (2014).
3. Ni, G. *et al.* Steam generation under one sun enabled by a floating structure with thermal concentration. *Nat. Energy* **1**, 16126 (2016).
4. Lee, J., Laoui, T. & Karnik, R. Nanofluidic transport governed by the liquid/vapour interface. *Nat. Nanotechnol.* **9**, 317-323 (2014).
5. Lynn, N. S. & Dandy, D. S. Passive microfluidic pumping using coupled capillary/evaporation effects. *Lab Chip* **9**, 3422-3429 (2009).
6. Li, D. *et al.* Enhancing flow boiling heat transfer in microchannels for thermal management with monolithically-integrated silicon nanowires. *Nano Lett.* **12**, 3385-3390 (2012).
7. Radha, B. *et al.* Molecular transport through capillaries made with atomic-scale precision. *Nature* **538**, 222-225 (2016).
8. Li, Y., Alibakhshi, M. A., Zhao, Y. & Duan, C. Exploring ultimate water capillary evaporation in nanoscale conduits. *Nano Lett.* **17**, 4813-4819 (2017).
9. Narayanan, S., Fedorov, A. & Joshi, Y. K. Interfacial transport of evaporating water confined in nanopores. *Langmuir* **27**, 10666-10676 (2011).
10. Eames, I. W., Marr, N. J. & Sabir, H. The evaporation coefficient of water: a review. *Int. J. Heat Mass Tran.* **40**, 2963-2973 (1997).
11. Barkay, Z. Dynamic study of nanodroplet nucleation and growth using transmitted electrons in ESEM. In *Nanodroplets* **18**, 51-72 (Springer: New York, 2013).
12. Chen, L., Yu, J. & Wang, H. Convex nanobending at a moving contact line: the missing mesoscopic link in dynamic wetting. *ACS Nano* **8**, 11493-11498 (2014).
13. Deng, Y., Chen, L., Yu, J. & Wang, H. Nanoscopic morphology of equilibrium thin water film near the contact line. *Int. J. Heat Mass Tran.* **91**, 1114-1118 (2015).
14. Mehrizi, A. A. & Wang, H. Evaporation-induced receding contact lines in partial-wetting regime on a heated substrate. *Int. J. Heat Mass Tran.* **124**, 279-287 (2018).
15. Rahman, A. Correlations in the motion of atoms in liquid argon. *Phys. Rev.* **136**, A405 (1964).
16. Akkus, Y. & Beskok, A. Molecular diffusion replaces capillary pumping in phase-change driven nanopumps. Preprint at <https://arxiv.org/abs/1804.06056> (2018).
17. Lu, Z., Narayanan, S. & Wang, E. N. Modeling of evaporation from nanopores with nonequilibrium and nonlocal effects. *Langmuir* **31**, 9817-9824 (2015).
18. Barker, J. A. & Pompe, A. Atomic interactions in argon. *Aust. J. Chem.*, **21**, 1683-1694 (1968).
19. Foiles, S. M., Baskes, M. I. & Daw, M. S. Embedded-atom-method functions for the fcc metals Cu, Ag, Au, Ni, Pd, Pt, and their alloys. *Phys. Rev. B* **33**, 7983 (1986).
20. Freund, J. B. The atomic detail of an evaporating meniscus. *Phys. Fluids* **17**, 022104 (2005).
21. Yd, S. & Maroo S. C. Origin of surface-driven passive liquid flows. *Langmuir* **32**, 8593-8597 (2016).

SUPPORTING INFORMATION

Molecular dynamics simulations.

Two systems are simulated. Except the number of fluid (Ar) atoms and the interaction between fluid and solid atoms, both systems are identical and subjected to same computational procedure. Systems have identical channel walls composed of (3240x2=6480) Platinum (Pt) atoms. Each wall has 4 solid layers and (1,0,0) crystal planes facing the liquid. The outermost layer of the walls is always fixed at their lattice positions. 4200 and 5775 fluid atoms are used in the first and second simulations, respectively. Numbers of fluid atoms are selected such that condensed phase is always attached to the channel inlets and outlets and the effective radius of curvature (based on a circular fit) at the interface is approximately the same for both systems, when the systems are isothermally equilibrated before the initiation of the heating/cooling process. Periodic boundary conditions are applied in all directions. Time step is 5 fs and each collected data is averaged for 2 ns. Lennard-Jones (L-J) 6-12 potential is used to model the interactions between Ar-Ar and Ar-Pt atoms with molecular diameters of $\sigma_{\text{Ar}} = 0.34$ nm, $\sigma_{\text{Ar-Pt}} = 0.3085$ nm, and depth of the potential wells of $\epsilon_{\text{Ar}} = 0.01042$ eV, $\epsilon_{\text{Ar-Pt}} = 0.00558$ eV for the first and $\epsilon_{\text{Ar-Pt}} = 0.0558$ for the second simulation (Maruyama1999). L-J potential is truncated with a cut-off distance of $3\sigma_{\text{Ar}}$. Embedded atom model is utilized for Pt-Pt atomic interactions¹⁹. Simulations are started from the Maxwell-Boltzmann velocity distribution for all atoms at 110 K. Nosé-Hoover thermostat is applied to all atoms (except the outermost Pt layers) for 15 ns to stabilize the system temperature at 110 K. Then, microcanonical ensemble is applied to Ar atoms for 15 ns to equilibrate the system, while solid atoms are still subjected to the thermostat. At the end of the isothermal stage, stable liquid/vapor Ar mixture is attained at 110 K. Then, equal energy injection/extraction (first simulation: $\dot{q}=11$ nW, second simulation: $\dot{q}=20$ nW) is applied to the wall atoms located at the heating/cooling zones for 40 ns. Other wall atoms are not allowed to vibrate in order to eliminate heat conduction through the solid wall. During heating/cooling, fluid atoms are subjected to microcanonical ensemble. At the end of heating/cooling period, statistically stable phase changing liquid/vapor interfaces are formed at both ends of the channel. The rates of the steady passive liquid flow from condensing interface to evaporating interface through the channel are calculated as ' 728.7 ± 20.3 #Ar/ns' and ' 504.4 ± 12.1 #Ar/ns' for the first and second simulations, respectively. As an experimental observation^{22,23}, molecular layering of fluid near a solid should be considered as a link to the real-world behavior of the system. During all simulations, molecular layering of Ar is verified in the proximity of the walls. Moreover, the distribution and magnitude of the density peaks are in good agreement with the results of ²⁴, where same L-J potential parameters were used. All simulations are carried out using Large-scale Atomic/Molecular Massively Parallel Simulator (LAMMPS)²⁵.

Modeling strategy.

A saturated liquid/vapor mixture has equal evaporation and condensation rates at the interface. To disturb the equilibrium, a pressure difference between the bulk vapor and the vapor just above the interface must be generated. In an enclosed system, evaporation can be favored by reducing the bulk vapor pressure or increasing the interface pressure. The first method can be applied by continuously removing the vapor phase from the system. If the mixture is composed of water and air, controlling of relative humidity is an example of this procedure as it was performed by the

recent experiments^{7,8}. However, application of this methodology is not practical for MD modeling. Due to the computational cost of MD simulations, only a limited number of atoms/molecules can be simulated within restricted time spans. Continuous removal of atoms/molecules would decrease the total number of fluid atoms during a simulation. Before the establishment of a steady evaporation, fluid atoms can be totally consumed or drop below a certain amount, for which statistical averaging will not yield trustable results. In addition, as a deterministic simulation method MD preserves the number of simulated atoms. Therefore, instead of a transient process, a steady-state process, which preserves the total number atoms/molecules, is more reliable. To realize this, we use the recently proposed phase change induced pumping mechanism¹⁶. At the evaporator part of this pump, a stable evaporating liquid/vapor interface forms. Continuous heating at this part increases the temperature at the interface. Consequently, evaporation is sustained by the increase of interface pressure instead of removing vapor atoms/molecules. Selection of fluid type is also critical. The number of vapor atoms in the gas phase should be large enough for accurate statistical averaging. Therefore, the selected liquid should have high vapor pressure. Water, which was used in the recent experiments^{7,8}, is not a good choice for MD simulations due to its relatively low volatility. For instance, saturated water mixture in equilibrium at room temperature has the ratio of 1/50,000 vapor to total water molecules, which is unfavorable for MD simulations conducted in nano-scale volumes. Therefore, our modeling strategy aims to construct steady-state evaporation of a high volatile liquid in order to realize a statistically reliable evaporation analysis.

Interface detection

In order to determine the liquid/vapor interface, simulation domain is divided into rectangular bins and average fluid density is calculated at each bin. Starting from the outer gas phase region, density of each bin is checked in longitudinal directions and the first bins, where the bin density exceeds the cut-off density, are marked as the liquid/vapor interface. Cut-off density is selected slightly higher than the density of the first minimum density peak in the liquid phase, which is approximately 23% and 21% of the average bulk liquid density within the channel for the first and second simulations, respectively. Selection of a higher cutoff density implies the existence of a non-physical vapor region within the bulk liquid, which prevents detection of a continuous liquid/vapor interface. However, selection of a lower cutoff density results in a larger liquid volume and thicker adsorbed layers, which does not affect proper prediction of the mobility of adsorbed layers. Moreover, it is worth mentioning that calculation of evaporation rate is independent of the interface selection in our computational setup due to the steady evaporation and associated steady passive liquid flow within the channel. Rate of evaporation is estimated by calculating the mass flow rate from the liquid state at the mid-channel in each simulation.

Mass flow through adsorbed region

Mass flow rate through a cross section area, A , is functions of density, ρ , and velocity, \vec{u} :

$$\dot{m} = \int (\rho \vec{u}) \cdot \vec{n} dA \quad (1)$$

where \vec{n} is the unit normal vector of the surface, across which the mass flow is calculated. Within the adsorbed layer, mass flow rate along the surface coordinate 's' can be expressed per unit channel depth as follows:

$$\dot{m}'|_s = \int_0^{\delta^*} (\rho \vec{u}) \cdot \vec{n} d\delta \quad (2)$$

where δ is the coordinate along the surface normal and δ^* is the thickness of the adsorbed layer. Mass flow rate at a specific 's' location can be calculated by approximating the above equation using rectangle rule of numerical integration, which requires summing the mass flow rates through the bins positioned at this 's' location (see Extended Data Fig. 4).

$$\dot{m}'|_s = \left(b \sum_i (\rho \vec{u})_i \right) \cdot \vec{n} \quad (3)$$

where b is the height of each bin. When the velocity vector ($\vec{u} = u\vec{i} + v\vec{j}$) and the unit normal vector ($\vec{n} = n_x\vec{i} + n_y\vec{j}$) are decomposed to its components in horizontal and vertical directions, equation (3) can be expressed in terms of the contributions of mass flow rate in the horizontal and vertical directions as follows:

$$\dot{m}'|_s = b \sum_i [(\rho u)_i n_x + (\rho v)_i n_y] \quad (4)$$

Uncertainty analysis

Density, velocities and temperature are sampled at every 2 ns and all the data collected between the two measurements is averaged, which yields a measurement uncertainty, ε , for each time averaged data, $\langle . \rangle$.

$$\rho = \langle \rho \rangle \pm \varepsilon_\rho \quad (5a)$$

$$u = \langle u \rangle \pm \varepsilon_u \quad (5b)$$

$$v = \langle v \rangle \pm \varepsilon_v \quad (5c)$$

$$T = \langle T \rangle \pm \varepsilon_T \quad (5d)$$

Uncertainties associated with density (ε_ρ), horizontal velocity (ε_u), vertical velocity (ε_v) and temperature (ε_T) are estimated by calculating the standard error of measurements, which is evaluated by dividing the standard deviation of measurements to the number of samples.

Mass flux is simply the multiplication of density and velocity. Estimation of mass flux has also associated uncertainty due to the time averaging.

$$\rho u = \langle \rho u \rangle \pm \varepsilon_{\rho u} \quad (6a)$$

$$\rho v = \langle \rho v \rangle \pm \varepsilon_{\rho v} \quad (6b)$$

Uncertainties of mass fluxes in horizontal and vertical directions are expressed in terms of the uncertainties of density and velocities as follows:

$$\varepsilon_{\rho u} = \sqrt{(\varepsilon_{\rho} u)^2 + (\varepsilon_u \rho)^2} \quad (7a)$$

$$\varepsilon_{\rho v} = \sqrt{(\varepsilon_{\rho} v)^2 + (\varepsilon_v \rho)^2} \quad (7b)$$

Mass flow rate through surface coordinate 's' is calculated using equation (4), where the mass flow rate under a specific surface coordinate 's' is the summation of horizontal and vertical mass fluxes through each bin positioned at the 's' location. Therefore, uncertainty of the mass flow rate depends on the uncertainties of mass fluxes at the contributing bins as shown in equation (8).

$$\dot{m}'|_s = b \left\langle \sum_i [(\rho u)_i n_x + (\rho v)_i n_y] \right\rangle \pm b \sqrt{\sum_i [(\varepsilon_{\rho u})_i n_x]^2 + [(\varepsilon_{\rho v})_i n_y]^2} \quad (8)$$

When equation (7) is inserted into equation (8), mass flow rate and its uncertainty can be expressed as the functions of the measured data and their measurement uncertainties as follows:

$$\dot{m}'|_s = b \left\langle \sum_i [(\rho u)_i n_x + (\rho v)_i n_y] \right\rangle \pm b \sqrt{\sum_i [(\varepsilon_{\rho} u)_i^2 + (\varepsilon_u \rho)_i^2] (n_x)^2 + [(\varepsilon_{\rho} v)_i^2 + (\varepsilon_v \rho)_i^2] (n_y)^2} \quad (9)$$

Kinetic limit of evaporation

Hertz was the first to put an upper bound for the evaporation rates using kinetic theory of gases²⁶. Later, Knudsen²⁷ derived the theoretical maximum rate of evaporation of a liquid into its own vapor in terms of intensive thermodynamic properties.

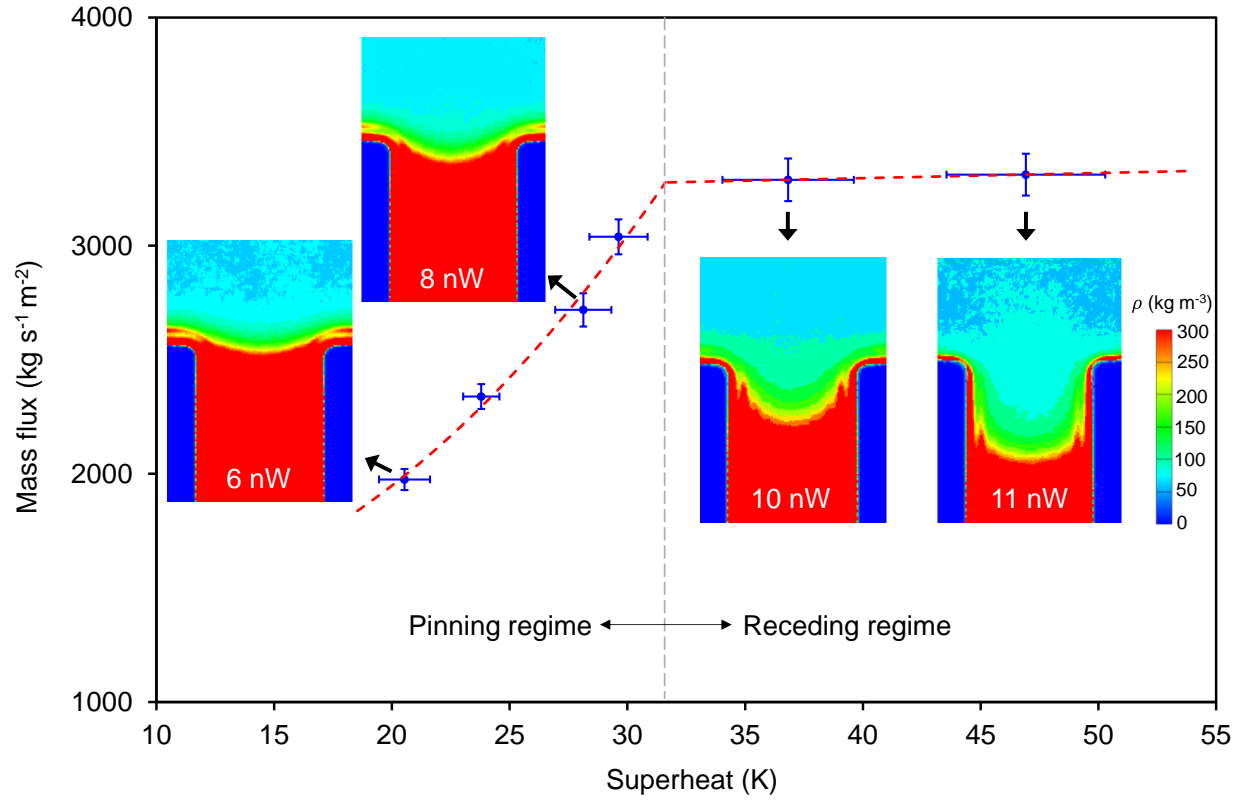
$$\dot{m}'' = \left(\frac{M}{2\pi R} \right)^{0.5} \left(\frac{p_{v,lv}}{\sqrt{T_{lv}}} - \frac{p_v}{\sqrt{T_v}} \right) \quad (10)$$

where M , R , T_{lv} , $p_{v,lv}$, T_v and p_v are molecular weight, universal gas constant, liquid/vapor interface temperature, vapor pressure just above the interface, vapor temperature and vapor pressure, respectively. This equation is known as Hertz-Knudsen (H-K) equation and widely used to predict the kinetic limit of evaporation flux at the liquid-vapor interface. Vapor pressure and temperature are measured away from the interface to capture the bulk properties of vapor. Interface temperature is calculated by averaging the temperature of the bins located at the interface. Interface pressure is taken as the equilibrium pressure of the vapor/liquid coexistence at the interface temperature.

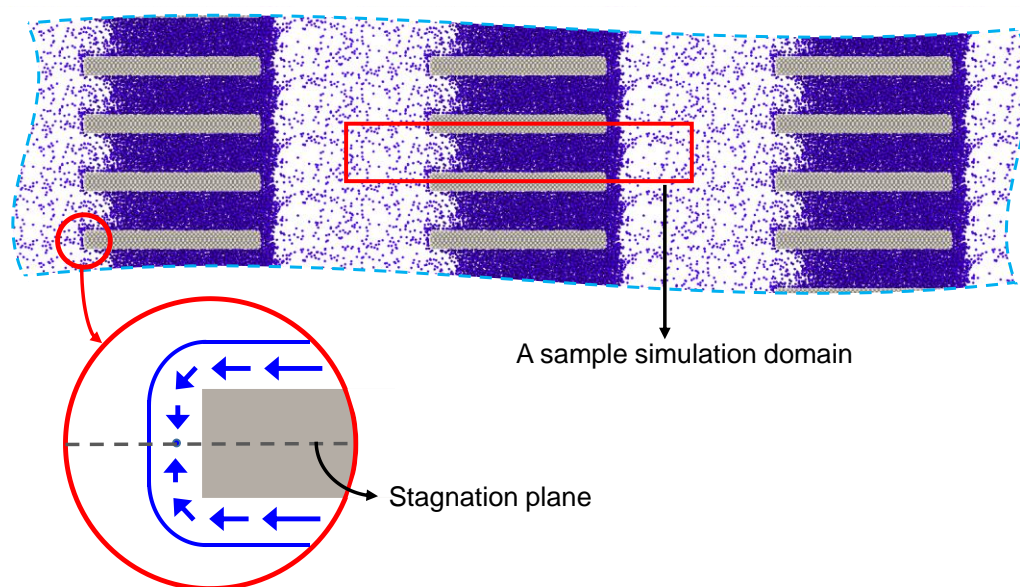
Supporting information - References

22. Heslot, F., Fraysse, N. & Cazabat, A. M. Molecular layering in the spreading of wetting liquid drops. *Nature* **338**, 640-642 (1989).
23. Cheng, L., Fenter, P., Nagy, K. L., Schlegel, M. L. & Sturchio, N.C. Molecular-scale density oscillations in water adjacent to a mica surface. *Phys. Rev. Lett.* **87**, 156103 (2001).
24. Maruyama, S. & Kimura, T. A study on thermal resistance over a solid-liquid interface by the molecular dynamics method. *Therm. Sci. Eng.* **7**, 63-68 (1999).
25. Plimpton, S. Fast parallel algorithms for short-range molecular dynamics. *J. Comput. Phys.* **117**, 1-19 (1995).
26. Hertz, H., *Ann. Phys.*, **253**, 177-193 (1882).
27. Knudsen, M., *The kinetic theory of gases* (Methuen, 1950).

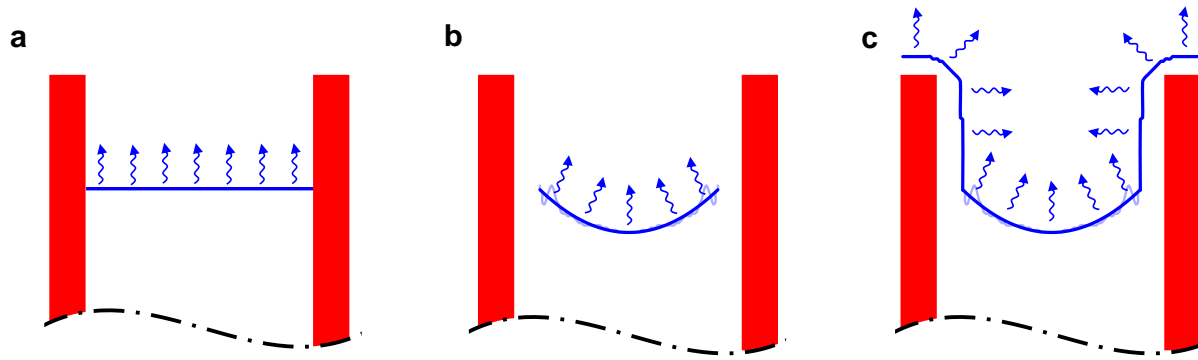
EXTENDED DATA FIGURES



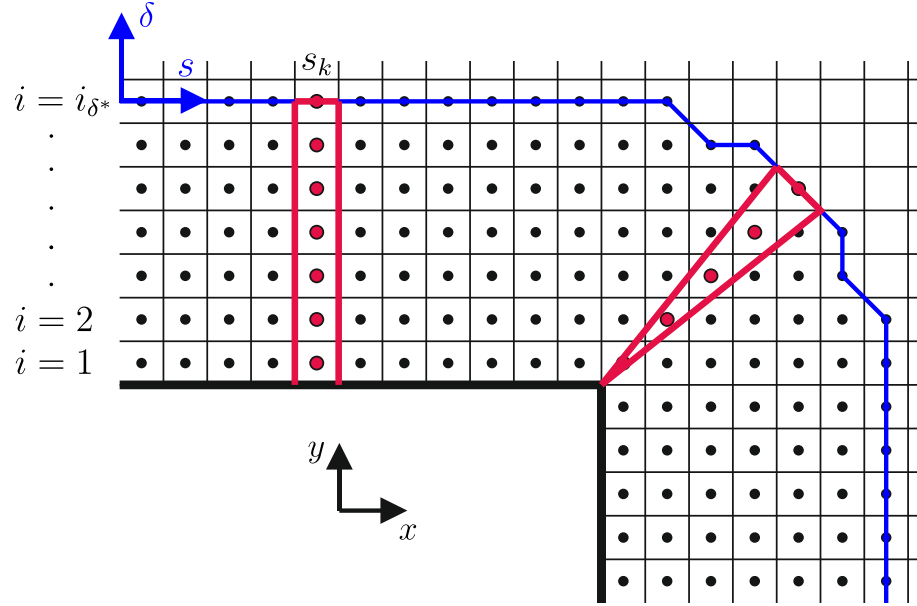
Extended Data Fig. 1 | Evaporative mass flux vs. superheat for the first simulation together with the location and profile of evaporating meniscus at different heating rates. Before heating, the system was isothermal and already equilibrated. Number of fluid atoms is selected such that liquid is attached to the channel inlets prior to heating. During simulations, different heating rates (\dot{q}) are applied to observe the response of evaporating meniscus. Heating rates above 6 nW yield apparent meniscus deformations. Between 6 nW and 9 nW, evaporative mass flux increases more than 50% in the expense of a 10 K superheat rise. However, after 10 nW, mass flux slightly increases, whereas the superheat elevates more than 10 K. To explain this behavior, morphology of the liquid/vapor interface is examined at the each heating rate. Between 6 nW and 9 nW, liquid meniscus was attached to the channel inlets. However, after 10 nW, the extended meniscus is detached from the channel tips and receded into channel. During the simulation with 12 nW heating, evaporation resistance experienced a jump, which is accepted as the indication of burnout and the simulation is ceased. Second order curve fittings (red dashed curves) applied to these data groups and two different regimes (pinning and receding) are identified. This regime shift were previously demonstrated by a recent study¹⁷, where the minimum nanopore modeled had a hydraulic diameter of 20 nm.



Extended Data Fig. 2 | A sample simulation domain and its neighboring periodic images. We used periodic boundary conditions (PBCs) at all boundaries of the simulation domain. Using PBCs has advantages such as eliminating the surface effects and keeping the same number of molecules within the simulation domain. On the other hand, application of PBCs in all directions is geometrically equivalent to replication of the simulation domain throughout the space to form an infinite lattice. For the sake of brevity, we included only the neighbor images to a sample simulation domain in the figure. The center plane of each wall is actually a stagnation zone due to the merging of two opposite streams. This stagnation plane and the opposing streams are emphasized in the close up view.



Extended Data Fig. 3 | Evaporation area selection. **a**, The cross sectional area between channel walls. The simplest and most common way is to take the cross sectional area of the conduit as the evaporation area. However, extended evaporating meniscus has larger surface area than cross sectional area, except in extremely small systems, where the adsorbed layer thickness is comparable with the system size. Therefore, this selection usually leads to an overestimation of heat fluxes. **b**, Extended meniscus area. Surface area of the meniscus extended between the adsorbed layers on the channel walls is calculated based on a curve fit (shown by solid blue line) to the liquid/vapor interface (shown by semi-transparent blue line). Estimated extended meniscus area is slightly smaller than the cross sectional area due to omission of the adsorbed layer. **c**, Liquid/vapor interfacial area including the adsorbed layer interface. Interfacial area of adsorbed layers on both channel walls are added to the extended meniscus area.



Extended Data Fig. 4 | Mass flow calculation through adsorbed region. The figure is plotted for demonstration purposes and it does not reflect the real adsorbed layers observed in simulations, which contain much higher number of bins. The dots show the center of each bin, where the flow properties are averaged in time. Blue line shows the liquid/vapor interface, which is formed by connecting the center of bins having higher density than the cut-off density (see Methods section ‘Interface detection’). Mass flow is calculated along this interface, i.e. along the surface coordinate ‘ s ’. Step size (arc length of interface at each step) is determined by connecting the mid points of two successive bin centers. Mass flow rate at each step is calculated by summing the mass flow rates of all bins located between the surface and wall (see Methods section ‘Mass flow through adsorbed region’). The red rectangle and the red dots within this region show contributing bins to the mass flow calculated at a certain step along the inner wall surface. The red triangle, on the other hand, specifies the contributing bins at a certain step at the corner region.